Supplementary Information

A tethered ligand assay to probe SARS-CoV-2:ACE2 interactions

Magnus S. Bauer[a,b,c,1], Sophia Gruber[a,b,1], Adina Hausch[a,b], Priscila S. F. C. Gomes[d], Lukas F. Millese[e,f], Thomas Nicolaus[a,b], Leonard C. Schendel[a,b], Pilar López Navajas[g], Erik Procko[h,i], Daniel Lietha[g], Marcelo C. R. Melo[d], Rafael C. Bernardi[d], Hermann E. Gaub[a,b], and Jan Lipfert[a,b,2]

[a]Department of Physics, LMU Munich, Munich, 80799 Germany;
[b]Center for NanoScience, LMU Munich, Munich, 80799 Germany;
[c]Department of Chemical Engineering, Stanford University, Stanford, CA 94305;
[d]Department of Physics, Auburn University, Auburn, AL 36849;
[e]Department of Biochemistry, University of Washington, Seattle, WA 98195;
[f]Institute for Protein Design, University of Washington, Seattle, WA 98195;
[g]Centro de Investigaciones Biológicas Margarita Salas, Spanish National Research Council, Madrid, 28040 Spain;
[h]Department of Biochemistry, University of Illinois, Urbana, IL 61801;
and [i]Cancer Center at Illinois, University of Illinois, Urbana, IL 61801

[1] M.S.B. and S.G. contributed equally to this work.
[2] To whom correspondence may be addressed. Email: jan.lipfert@lmu.de.

The Supplementary Information contains SI Materials and Methods, Full Protein Sequences, Tables 1-4 and Supplementary Figures S1-S7

Supplementary Fig. 1	Full force extension curve of the tethered ligand protein construct including the RBD of SARS-CoV-2 and ACE2
Supplementary Fig. 2	Disulfide bridges shield large parts of the SARS-CoV-1 and SARS-CoV-2 RBD structure
Supplementary Fig. 3	Unfolding of ACE2 by AFM SMFS
Supplementary Fig. 4	ACE2 unfolding events observed in different constructs in the MT
Supplementary Fig. 5	Dwell time analysis of the tethered ligand extension time traces in MT
Supplementary Fig. 6	Dynamic force spectrum of the SARS-CoV-2 RBD:ACE2 dissociation
Supplementary Fig. 7	Depiction of the interface between SARS-CoV-1 RBD and ACE2

MATERIALS AND METHODS

All chemicals used were supplied by Carl Roth (Karlsruhe, Germany) or Sigma-Aldrich (St. Louis, MO, USA) unless otherwise noted.

Cloning and protein construct design

Constructs for ACE2-linker-RBD of SARS-CoV-1 were designed in SnapGene Version 4.2.11 (GSL Biotech LLC, San Diego, CA, USA) based on a combination of the ACE2 sequence from Komatsu et al. (1) available from GenBank under accession number AB046569 and the SARS-CoV-1 sequence from Marra et al. (2) available from GenBank under accession number AY274119. The crystal structure by Li et al. (3) available from the Protein Data Bank (PDB ID: 2ajf) was used as a structural reference. The linker sequence and tag placement were adapted from Milles et al. (4). The linker sequence is a combination of two sequences available at the iGEM parts databank (accession numbers BBa_K404300, BBa_K243029). We used a similar approach to design the fusion protein with the sequence of the RBD of SARS-CoV-2 from the sequence published by Wu et al. (5) available from GenBank under accession number MN908947. A 6x histidine (His) tag was added for purification. In addition, tags for specific pulling in magnetic tweezers and the atomic force microscope were introduced: a triple glycine for sortase-mediated attachment on the N-terminus and a ybbR-tag, AviTag, and Fgɣ tag on the C-terminus. In summary, the basic construct is built up as follows: MGGG-ACE2-linker-RBD-6xHIS-ybbR-AviTag-Fgɣ. All protein sequences are provided in the full protein sequences paragraph.

The constructs were cloned using Gibson assembly from linear DNA fragments (GeneArt, ThermoFisher Scientific, Regensburg, Germany) containing the sequence of choice codon-optimized for expression in E. coli into a Thermo Scientific pT7CFE1-NHis-GST-CHA Vector (Product No. 88871). The control construct with a different sized linker and just ACE2 were obtained by blunt end cloning adding additional residues to the linker or deleting parts of the construct. Replication of DNA plasmids was obtained by transforming in DH5-Alpha Cells and running overnight cultures with 7 ml lysogeny broth with 50 µg/ml carbenicillin. Plasmids were harvested using a QIAprep® Spin Miniprep Kit (QIAGEN, Germantown, MD, USA, # 27106).

In vitro protein expression

Expression was conducted according to the manual of 1-Step Human High-Yield Mini in vitro translation (IVT) kit (# 88891X) distributed by ThermoFisher Scientific (Pierce Biotechnology, Rockford, IL, USA). All components, except 5X dialysis buffer, were thawed on ice until completely thawed. 5X dialysis buffer was thawed for 15 minutes and 280 µl were diluted into 1120 µl nuclease-free water to obtain a 1X dialysis buffer. The dialysis device provided was placed into the dialysis buffer and kept at room temperature until it was filled with the expression mix.

For preparing the IVT expression mix, 50 µl of the HeLa lysate was mixed with 10 µl of accessory proteins. After each pipetting step, the solution was gently mixed by stirring with the pipette. Then the HeLa lysate and accessory proteins mix was incubated for 10 minutes. Afterwards, 20 µl of the reaction mix was added. Then 8 µl of the specifically cloned DNA (0.5 µg/µl) was added. The reaction mix was then topped off with 12 µl of nuclease-free water to obtain a total of 100 µl. This mix was briefly centrifuged at 10,000 g for 2 minutes. A small white pellet appeared. The supernatant was filled into the dialysis device placed in the 1X dialysis buffer. The entire reaction was then incubated for 16 h at 30°C under constant shaking at 700 rpm. For incubation and shaking a ThermoMixer comfort 5355 (Eppendorf AG, Hamburg, Germany, # 5355) with a 2 ml insert was used. After 16 h the expression mix was removed and stored in a protein low binding reaction tube on ice until further use.

Protein purification

Purification was conducted using HIS Mag Sepharose® Excel beads (Cytiva Europe GmbH, Freiburg, Germany, # 17371222) together with a MagRack™ 6 (Cytiva Europe GmbH, Freiburg, Germany, # 28948964) following the provided protocol. Bead slurry was mixed thoroughly by vortexing. 200 µl of homogenous beads were dispersed in a 1.5 ml protein low binding reaction tube. Afterwards the reaction tube was placed in the magnetic rack and the stock buffer was removed. Next, the beads were washed with 500 µl of HIS wash buffer (25 mM TRIS-HCl, 300 mM NaCl, 20 mM imidazole, 10% vol. glycerol, 0.25 % vol. Tween 20, pH 7.8). Expressed protein from IVTT was filled to 1000 µl with TRIS buffered saline (25 mM TRIS, 72 mM NaCl, 1 mM $CaCl_2$, pH 7.2) and mixed with freshly washed beads. The mix was incubated in a shaker for 1 h at room temperature. Subsequently, the reaction tube was placed in the magnetic rack and the liquid was removed. The beads were washed three times with wash buffer, keeping the total incubation time to less than 1 min. Remaining wash buffer was removed and 100 µl elution buffer (25 mM TRIS-HCl, 300 mM NaCl, 300 mM imidazole, 10% vol. glycerol, 0.25 % vol. Tween 20, pH 7.8) were added to wash protein off the beads. The bead elution buffer mix was then incubated for one minute with occasional gentle vortexing. Afterward, the reaction tube was placed in the magnetic rack again to remove the eluted protein. This step was repeated for a second and third elution step. The buffer of the eluted protein was exchanged to TRIS buffered saline (TBS - 25mM TRIS, 72mM NaCl, 1mM $CaCl_2$ at pH 7.2) in 0.5 ml 40k Zeba spin columns distributed by ThermoFisher Scientific (Pierce Biotechnology, Rockford, IL, USA, # 87767) or 0.5 ml 50k Amicon Centrifugal Filters (Merck KGaA, Darmstadt, Germany, #UFC5050BK). Concentrations were determined photospectrometrically with a NanoDrop and aliquots were frozen in liquid nitrogen.

Atomic force microscopy setup

The AFM force spectroscopy datasets were collected on a custom-built AFM based on an MFP3D controller (Asylum Research, Santa Barbara, CA, USA). The AFM head was kept stationary, while the sample stage was moved by an xyz-movable piezo-driven sample stage (P-313.30D - P-313 PicoCube® XY(Z)-Piezoscanner - Physik Instrumente PI GmbH & Co KG, Karlsruhe, Germany) together with a high-precision xy-nanopositioner (P-621.2CD - Physik Instrumente PI GmbH & Co KG, Karlsruhe, Germany). Unfolding traces were recorded by (i) approaching the functionalized sample surface onto the functionalized cantilever until the cantilever is indented with 180 pN into the surface, allowing the linkage between ClfA:Fgɣ to form; (ii) retraction of the cantilever with 0.8 µm/s (except for the dynamic force spectrum recorded at additional speeds of 0.4 µm/s, 1.6 µm/s and 3.2 µm/s) while recording the deflection of the cantilever to obtain a force distance curve of the mechanical response of the protein probed; (iii) after the surface moved 500 nm in z direction (assuming a complete unfolding) a new position is set by the xy-stage, moving the sample surface horizontally by steps of 100 nm in a spiral pattern and starting a new acquisition process in step (i). This process is operated by a software programmed in IgorPro6 (Wavemetrics, Portland, OR, USA) and the unfolding curves obtained are saved in an hdf5 file.

For calibration the Inverse Optical Cantilever Sensitivity (InvOLS) was obtained by 25 hard indentation curves allowing to correlate the movement of the cantilever with the voltage signal recorded on a quadrant photodetector. The spring constants of the cantilevers were calibrated based on thermal fluctuations using the equipartition theorem method (6, 7) resulting in spring constants around 100 pN/nm. The spring constant per measurement are listed below. To be able to directly compare force values recorded with different cantilevers, the ACE2 fingerprint pattern was used to normalize the force histograms.

In the course of a measurement around 50,000 - 400,000 force-distance traces were recorded. Most force-distance traces didn't show any interactions and only a fraction showed specific single-molecule unfolding events.

List of spring constants (k) of cantilevers used for individual measurements used for comparing forces and contour length increments:

SARS-CoV-2 measurement - Figure 2A (exemplary curve), C and Supplementary Figure S1

$k = 101.4$ pN/nm

SARS-CoV-1 short linker (31 nm) measurement - Figure 2B
k = 108.0 pN/nm

SARS-CoV-1 long linker (42 nm) measurement - Figure 2B top only
k = 109.5 pN/nm

Ectodomain of ACE2 - Supplementary Figure S3
k = 96.0 pN/nm

Dynamic force spectrum - Supplementary Figure S6
k = 97.6 pN/nm

AFM surface and cantilever preparation

Cantilevers and sample surfaces were both silanized for further functionalization steps. Surface attachment and linkage was obtained by 5,000 Da heterobifunctional NHS-PEG-Maleimide spacers (Rapp Polymere, Tübingen, Germany, # 135000-65-35). Specific protein attachment was achieved using a sortase-mediated reaction on the sample surface and an 4'-phosphopantetheinyl transferase (sfp)-mediated reaction for the AFM cantilever ensuring a well-defined pulling geometry.

The cantilevers (BioLever mini, BL-AC40TS) were oxidized in an UV ozone cleaner (UVOH 150 LAB; FHR Anlagenbau GmbH, Ottendorf-Okrilla, Germany) and after that silanized for 2 min in 50% (vol/vol) ethanol and (3-aminopropyl)dimethylethoxysilane (abcr GmbH, Karlsruhe, Germany, AB146193, CAS 18306-79-1). To rinse off the residual silane cantilevers were stirred in 2-Propanol (IPA) and in Milli-Q. After that the cantilevers are dried at 80°C for 30 min. The heterobifunctional PEG spacers are solved in 100 mM HEPES (pH 7.4) to 50 mM. The cantilevers were incubated in droplets of PEG dissolved in 100 mM HEPES (pH 7.4) to 50 mM for 1 h. After a rinsing step the cantilevers are incubated in 20 mM Coenzyme A (CoA) (# 234101-100MG, Calbiochem distributed by Sigma-Aldrich) dissolved in coupling buffer (50 mM disodium phosphate buffer, 50 mM NaCl, 10 mM EDTA, pH 7.2). for 1 h. Droplets with a mixture of 2 µM sfp, 100 mM $MgCl_2$ and 60 µM ClfA (in TBS buffer) are prepared to attach the ybbR tag of ClfA specifically to CoA. The cantilevers are incubated in these droplets for at least 1.5 h. To prepare the cantilevers for the measurement they are rinsed and stored in TBS.

Glass surfaces are cleaned by sonication in 50% (vol/vol) IPA in Milli-Q for 15 min. To prime the surfaces for silanization they are incubated for 30 min in a solution of 50% (vol/vol) hydrogen peroxide (30%) and sulfuric acid (“piranha solution”). To wash off the residual solution the surfaces are washed in Milli-Q and dried under a constant stream of N2. For the actual silanization step the surfaces are incubated in 1.8% (vol/vol) ethanol and (3-aminopropyl)dimethylethoxysilane (abcr GmbH, Karlsruhe, Germany, AB146193, CAS 18306-79-1). Afterwards the surfaces are washed with IPA and Milli-Q and dried at 80°C for 45 min. To minimize sample volumes for the following incubations silicone incubation wells (CultureWell reusable gaskets, Grace Bio-Labs, Bend, OR, USA, # 103250) are placed centered on the pre-treated surfaces. Then heterobifunctional PEG spacers are dissolved in 100 mM HEPES (pH 7.4) to 50 mM and applied to the wells for 1 h. Subsequently the surfaces are rinsed with Milli-Q and 5 mM Cys-LPETGG in coupling buffer (sodium phosphate, pH 7.2) is pipetted into the wells and incubated for 2 h. After washing the wells with Milli-Q, the purified tethered ligand protein is applied in solution together with 1 µM sortase and 10 mM CaCl2 for 25 min. After incubation the incubation wells are removed and the surface is rinsed with 10 ml TBS.

To validate the functionalization of the cantilever and the surfaces for each measurement (for each new surface and cantilever), a control surface of the same surface batch is prepared with a GGG-ddFLN4-Fgɣ construct using identical procedures as for the sample surface.

AFM data analysis

Data analysis was carried out in custom Python 2.7 (Python Software Foundation, Wilmington, DE, USA) scripts (8-10) and Python 2.7-based Jupyter notebooks (11). The rupture forces were detected by a peak detection that highlights drops above the baseline noise level in total variation denoised (TVD) force-distance traces. A linear slope in force vs. time was used to determine the loading rate, taking into account 4 nm before each rupture event. Rupture forces of the peaks in the unfolding pattern were binned to histograms and fitted with the Bell-Evans model yielding the most probable rupture force (12).

All curves showing the characteristic unfolding pattern of the tethered ligand protein were aligned (accounting for the inhomogeneity in PEG lenghts) and assembled to heatmaps to visualize the recurring, characteristic unfolding pattern. The heatmaps contain the raw unfolding curves in force-distance space binned in 90 bins in both x- and y-axis between -10 pN to 60 pN and -10 nm to 300 nm.

To transform force-extension data into contour length space (13) a three-regime model by Livadaru et. al (14) assuming a stiff element of b = 0.11 nm and bond angle $\gamma = 41°$ was used. A Gaussian kernel density estimate, with a bandwidth of 4 nm, was applied to the contour length data to obtain density curves of each trace. These curves were aligned in contour length space using the following process previously described by Baumann et al. (15): "the full set of transformed force-distance curves is aligned to a random curve from this data set according to least residual in cross-correlation. This process results in a first superposition which is used as a template in a second iteration of this process. Again, all contour-length transformed curves are aligned to a template curve but this time to the one formed by the first iteration. This two-step approach diminishes biasing effects given by the choice of the random curve used for initial alignment. Contour lengths of the individual domains are determined by a Gaussian fit of each determined peak and subtraction of the respective fitted means." The datasets can be found at figshare (https://doi.org/10.6084/m9.figshare.15062373.v1) together with all analysis scripts at github (https://github.com/magnusbauer/AFM-CoV-2) executable with all datasets in google colab (https://colab.research.google.com/github/magnusbauer/AFM-CoV-2/blob/main/AFM_analysis.ipynb).

Molecular dynamic simulation

To examine the stability of the protein complex under mechanical load, we carried out steered molecular dynamics simulations employing NAMD 3 (16). Simulations were prepared using VMD (17) and its QwikMD (18) molecular dynamics interface. The structure of the complexes were prepared following established protocols (19). For the SARS-CoV-1 RBD:ACE2 complex, the structure had been solved by X-ray crystallography at 2.90 Å resolution and is available at the protein data bank (PDB ID: 2ajf) (3). The SARS-CoV-2 RBD:ACE2 complex had been similarly solved by X-ray crystallography, at 2.45 Å resolution, and is available at the protein data bank (PDB ID: 6m0j) (20). SARS-CoV-1 RBD or SARS-CoV-2 RBD and the ectodomain of human ACE2 were joined by flexible polypeptide linkers. The structure of the complexes with the linkers was obtained using Modeller (21) and fitted with VMD (17). Disulfide bonds were included following the literature information (22).

Employing advanced run options of QwikMD, structural models were solvated and the net charge of the proteins were neutralized using a 75 mM salt concentration of sodium chloride, which were randomly arranged in the solvent. The overall number of atoms included in MD simulations varied from approximately 200,000 in the RDB:ACE2 systems with no linker, to nearly 4,000,000 in the systems RDB:ACE2 connected by flexible polypeptide linkers. All simulations were performed employing the NAMD molecular dynamics package (16), and run on NVIDIA DGX-A100-based cluster nodes at Auburn University. The CHARMM force field (23, 24) along with the TIP3 water model (25) was used to describe all systems. The simulations were performed assuming periodic boundary conditions in the NpT ensemble with temperature maintained at 300 K using Langevin dynamics for pressure, kept at 1 bar, and temperature coupling. A distance cut-off of 12.0 Å was applied to short-range, non-bonded interactions, whereas long-range electrostatic interactions were treated using the particle-mesh Ewald (PME) (26) method. The equations of motion were integrated using the r-RESPA multiple time step scheme (27) to update the van der Waals interactions every two steps and electrostatic interactions every four steps. The time step of integration was chosen to be 4 fs for all production simulations performed, and 2 fs for all equilibration runs. For the 4 fs simulations, hydrogen mass repartitioning was done using psfgen in VMD. Before the MD simulations all the systems were submitted to an energy minimization protocol for 5,000 steps.

MD simulations with position restraints in the protein backbone atoms were performed for 1.0 ns and served to pre-equilibrate systems before the 10 ns equilibrium MD runs, which served to evaluate structural model stability. During the 1.0 ns pre-equilibration the initial temperature was set to zero and was constantly increased by 1 K every 1,000 MD steps until the desired temperature (300 K) was reached.

In all simulations, totaling over 300 SMD simulations, SMD was employed by harmonically restraining the position of a terminal amino acid residue, and moving a second restraint point, at a terminal amino acid residue of the other domain, with constant velocity in the +z direction. The procedure is equivalent to attaching one end of a harmonic spring to the end of a domain and pulling on the other end of the spring. The force applied to the harmonic spring is then monitored during the time of the molecular dynamics simulation. The pulling point was moved with constant velocity along the z-axis and due to the single anchoring point and the single pulling point the system is quickly aligned along the z-axis. Owing to the flexibility of the linkers between the RDB:ACE2 and fingerprint domains, this approach mimics the experimental set-up. The SMD simulations (28) were performed using the constant velocity stretching (SMD-CV) protocol, with pulling velocity 12.5 and 2.5 Å/ns. In our *in silico* SMFS approach, many replicas of simulations performed (at least 24 per system). Values for the force on the pulling spring were saved every 50 steps. The spring constant of the pulling spring was set to 5.0 kcal/mol/Å, while the holding spring had a constant of 100 kcal/mol/Å. Analyses of MD trajectories were carried out employing VMD (17) and its plug-ins, as well as in-house python-based Jupyter notebooks (11). Secondary structures were assigned using the Timeline plug-in, which employs STRIDE criteria. Force propagation profiles (29) were analysed using generalized cross correlation-based network analysis (30). A network was defined as a set of nodes, all α-carbons in our case, with connecting edges. Edges connect pairs of nodes if corresponding monomers are in contact, and 2 non-consecutive monomers are said to be in contact if they fulfil the proximity criterion that, namely any heavy atoms (non-hydrogen) from the 2 monomers are within 4.5 Å of each other for at least 75% of the frames analyzed.

Chimera protein construction

The structures of SARS-CoV-1 and SARS-CoV-2 RBDs complexed with human ACE2 were retrieved from the Protein Data Bank; PDB IDs: 2ajf and 6m0j, respectively. The RBD:ACE2 protein interfaces were investigated using PDBsum (31) and were visually inspected using VMD (17) to compare the amino-acid differences between SARS-CoV-1 and SARS-CoV-2. Modeller (21) was employed to construct the model for SARS-CoV-1 chimera based on the structure of SARS-CoV-1 (PDB ID: 2ajf) taking into account the residue substitutions on the SARS-CoV-2 RBD:ACE2 interface (Supplementary Table 3). Crystallographic water molecules and Zn^{2+} ions were kept in place while other heteroatoms were removed. Residues 376-381 that are missing in the crystallographic structure were included on the model using Modeller.

Magnetic tweezers instrument

Measurements were performed on a custom MT setup described previously (32, 33). In the setup, molecules are tethered in a flow cell (FC; see next section); mounted above the FC is a pair of permanent magnets (5×5×5 mm^3 each; W-05-N50-G, Supermagnete, Gottmadingen, Germany) in vertical configuration (34). The distance between magnets and FC is controlled by a DC-motor (M-126.PD2, Physik Instrumente PI GmbH & Co KG, Karlsruhe, Germany) and the FC is illuminated by an LED (69647, Lumitronix LED Technik GmbH, Germany). Using a 40x oil immersion objective (UPLFLN 40x, Olympus, Japan) and a CMOS sensor camera with 5120 x 5120 pixels (5120 x 5120 pixels, CP80-25-M-72, Optronis, Kehl, Germany) a field of view of approximately 680 × 680 μm^2 is imaged at a frame rate of 72 Hz. To control the focus and to create the look-up table required for tracking the bead positions in z, the objective is mounted on a piezo stage (Pifoc P-

726.1CD, Physik Instrumente PI GmbH & Co KG, Karlsruhe, Germany). Images are transferred to a frame grabber (microEnable 5 ironman VQ8-CXP6D, Silicon Software, Mannheim, Germany) and analyzed with an open-source tracking software (35, 36). The tracking accuracy of our setup was determined to be ≈ 0.6 nm in (x, y) and ≈ 1.5 nm in z direction, as determined by tracking non-magnetic polystyrene beads, after baking them onto the flow cell surface. Force calibration was performed as described (37) by analysis of the fluctuations of long DNA tethers. Importantly, for the small extension changes on the length scales of our protein tethers, the force stays constant to very good approximation (to better than 10^{-4} relative change (32)). The largest source of force uncertainty is due to bead-to-bead variation, which is on the order of ≤ 10% for the beads used in this study (34, 38).

Flowcell preparation and magnetic tweezers measurements

Flowcells (FCs) were prepared as described previously (32). For the bottom slides, high precision microscope cover glasses (24 mm x 60 mm x 0.17 mm, Carl Roth) were amino-silanized for further functionalization (equal to AFM surface preparation). They were coated with sulfo-SMCC (39) (sulfosuccinimidyl 4-(N-maleimidomethyl)cyclohexane-1-carboxylate; sulfo-SMCC, ThermoFisher Scientific, Pierce Biotechnology, Rockford, IL, USA, # 22322). For this purpose, 180 µl sulfo-SMCC (10 mM in 50 mM Hepes buffer, pH 7.4) was applied to one amino-silanized slide that was sandwiched with another slide and incubated for 45 min. Unbound sulfo-SMCC was removed by rinsing with Milli-Q. Next, elastin-like polypeptide (ELP) linkers (40) with a sortase motif at their C-terminus were coupled to the maleimide of the sulfo-SMCC via a single cysteine at their N-terminus, by sandwiching two slides with 100 µl ELP linkers (in 50 mM Disodium phosphate buffer with 50mM NaCl and 10mM EDTA, pH 7.2) and incubating them for 60 min. Subsequently, after further Milli-Q rinsing to remove unbound ELP linkers, free sulfo-SMCC was neutralized with free cysteine (10 mM in 50 mM disodium phosphate buffer with 50 mM NaCl and 10 mM EDTA, pH 7.3). 1 µm diameter polystyrene beads dissolved in ethanol were applied to the glass slides. After the ethanol evaporated, beads were baked onto the glass surface for 5 min at ≈ 80°C to serve as reference beads during the measurement. FCs were assembled from an ELP-functionalized bottom slide and an unfunctionalized high-precision microscope cover glass slide with two holes (inlet and outlet) on either side serving as top slide. Both slides were separated by a layer of parafilm (Pechiney Plastic Packaging Inc., Chicago, IL, USA), which was cut out to form a 50 µl channel. FCs were incubated with 1% (v/v) casein solution (# C4765-10ML, Sigma-Aldrich) for 2 h and flushed with 1 ml buffer (25 mM TRIS, 72 mM NaCl, 1 mM CaCl2, pH 7.2 at room temperature).

CoA-biotin (# S9351 discontinued, New England Biolabs, Frankfurt am Main, Germany) was coupled to the ybbR-tag at the C-terminus of the fusion protein constructs in a 90 - 120 min bulk reaction in the presence of 4 µM sfp phosphopantetheinyl transferase (41) and 100 mM $MgCl_2$ at room temperature (≈ 22°C). Proteins were diluted to a final concentration of about 50 nM in 25 mM TRIS, 72 mM NaCl, 1 mM $CaCl_2$, pH 7.2 at RT. To couple the N-terminus of the fusion proteins carrying three glycines to the C-terminal LPETGG motif of the ELP-linkers, 100 µl of the protein mix was flushed into the FC and incubated for 24 min in the presence of 1.3 µM evolved pentamutant sortase A from Staphylococcus aureus (42, 43). Unbound proteins were flushed out with 1 ml measurement buffer (25 mM TRIS, 72 mM NaCl, 1 mM CaCl2, 0.1% (v/v) Tween-20, pH 7.2). Finally, commercially available streptavidin-coated paramagnetic beads (Dynabeads™ M-270 Streptavidin, Invitrogen, Life Technologies, Carlsbad, CA, USA) were added into the FC and incubated for 30 s before flushing out unbound beads with 1 ml measurement buffer. Receptor-ligand binding and unbinding under force was systematically investigated by subjecting the protein tethers to (2 - 30) min long plateaus of constant force, which was gradually increased in steps of 0.2 or 0.3 pN. All measurements were conducted at room temperature.

For blocking measurements, recombinant human ACE2 (Gln18-Ser740, C-terminal His-tag) from RayBiotech (Peachtree Corners, GA, USA, # 230-30165-100 distributed by antibodies-online GmbH, Aachen, Germany, # ABIN6952473) was dissolved in measurement buffer for a final concentration of ~3.8 µM. Dissolved ACE2 was spun down in a tabletop centrifuge at 4°C, 14,000 rcf for 5 min to avoid introduction of larger particles into the FC that could influence video tracking. 80 µl ACE2 were flushed into the FC and shortly incubated before applying 7 pN to force dissociation of the tethered ligand construct and allow the free ACE2 to bind. Afterwards, a measurement was conducted in the presence of free ACE2.

Data analysis of MT traces

MT traces were selected on the basis of the characteristic ACE2 two-step unfolding pattern above 25 pN, conducted at the end of each experiment. For each trace, (x,y)-fluctuations were also checked to avoid inclusion of tethers that exhibit inter-bead or bead-surface interactions, which would also cause changes in x or y. Non-magnetic reference beads were tracked simultaneously with magnetic beads and reference traces were subtracted for all measurements to correct for drift. Extension time traces were smoothed to one second with a moving average filter to reduce noise. All analyses were performed with custom scripts in MATLAB.

Estimate of forces on viral particles at the cell surface

The human respiratory system is covered with a thin layer of mucus (44). This layer exerts drag forces on virus particles bound to receptors. A simple upper estimate of the drag forces can be computed as follows: $F = \gamma \bullet v_{fluid}$ with $\gamma = 3\pi\eta r$ being the Einstein drag coefficient, η being the viscosity of the mucus layer, and r being the radius of the viral particle, in the case of SARS-CoV-2 r is in the range (60 nm – 140 nm) (45). The rheology of human respiratory mucus has been characterized and values for the viscosity lie in the range of h ~ (1 Pa•s – 100 Pa•s) (44). Estimations for the velocity of particle clearance in the airways suggest velocities in the range of v ~ (4 µm/s – 14 µm/s) (46). Thus, an upper estimation of the relevant drag forces acting on a stationary virus particle in the human respiratory tract is F ~ (2 pN – 2 nN).

The cellular cytoskeleton can generate forces greater than 40 pN on a single bond with extracellular ligands (47). Forces in cellular adhesions can span 10-100 pN which can comparably be applied to an attached viral capsid (48-50). Cellular dynamics generate loading velocities of micrometers per minute (51) leading to force loading rates of 1 to 10□ pN/s (52, 53) that can cause mechanical loading on a cell:virus bond. This sets the conditions viruses have to likely withstand to be able to stay attached to cells (54).

FULL PROTEIN SEQUENCES

RBD of SARS-CoV-1
RBD of SARS-CoV-2
ACE2

85 aa linker
115 aa linker
Sortase N-Tag
His6-Tag
ybbR
Avitag
Fgɣ

pT7CFE1-MGGG-ACE2-85aa-linker-SARS-CoV-1-RBD-HIS-ybbr- AviTag-Fgɣ

MGGGSSSTIEEQAKTFLDKFNHEAEDLFYQSSLASWNYNTNITEENVQNMNNAGDKWSAFLKE
QSTLAQMYPLQEIQNLTVKLQLQALQQNGSSVLSEDKSKRLNTILNTMSTIYSTGKVCNPDNP
QECLLLEPGLNEIMANSLDYNERLWAWESWRSEVGKQLRPLYEEYVVLKNEMARANHYEDYGD
YWRGDYEVNGVDGYDYSRGQLIEDVEHTFEEIKPLYEHLHAYVRAKLMNAYPSYISPIGCLPA
HLLGDMWGRFWTNLYSLTVPFGQKPNIDVTDAMVDQAWDAQRIFKEAEKFFVSVGLPNMTQGF
WENSMLTDPGNVQKAVCHPTAWDLGKGDFRILMCTKVTMDDFLTAHHEMGHIQYDMAYAAQPF
LLRNGANEGFHEAVGEIMSLSAATPKHLKSIGLLSPDFQEDNETEINFLLKQALTIVGTLPFT
YMLEKWRWMVFKGEIPKDQWMKKWWEMKREIVGVVEPVPHDETYCDPASLFHVSNDYSFIRYY
TRTLYQFQFQEALCQAAKHEGPLHKCDISNSTEAGQKLFNMLRLGKSEPWTLALENVVGAKNM
NVRPLLNYFEPLFTWLKDQNKNSFVGWSTDWSPYADGATSGGGGSAGGSGSGSSGGSSGASGT
GTAGGTGSGSGTGSGGGSGGGSEGGGSEGGGSEGGGSEGGGSEGGGSGGGSESGGSSARVVPS
GDVVRFPNITNLCPFGEVFNATKFPSVYAWERKKISNCVADYSVLYNSTFFSTFKCYGVSATK
LNDLCFSNVYADSFVVKGDDVRQIAPGQTGVIADYNYKLPDDFMGCVLAWNTRNIDATSTGNY
NYKYRYLRHGKLRPFERDISNVPFSPDGKPCTPPALNCYWPLNDYGFYTTTGIGYQPYRVVVL
SFELLNAPATVCGPKLSTDLIKNQCVNFSGHHHHHHTDSLEFIASKLAASGLNDIFEAQKIEW
HEGSGEGQQHHLGGAKQAGDV*

pT7CFE1-MGGG-ACE2-85aa-linker-SARS-CoV-2-RBD-HIS-ybbr-AviTag-Fgɣ

MGGGSSSTIEEQAKTFLDKFNHEAEDLFYQSSLASWNYNTNITEENVQNMNNAGDKWSAFLKE
QSTLAQMYPLQEIQNLTVKLQLQALQQNGSSVLSEDKSKRLNTILNTMSTIYSTGKVCNPDNP
QECLLLEPGLNEIMANSLDYNERLWAWESWRSEVGKQLRPLYEEYVVLKNEMARANHYEDYGD
YWRGDYEVNGVDGYDYSRGQLIEDVEHTFEEIKPLYEHLHAYVRAKLMNAYPSYISPIGCLPA
HLLGDMWGRFWTNLYSLTVPFGQKPNIDVTDAMVDQAWDAQRIFKEAEKFFVSVGLPNMTQGF
WENSMLTDPGNVQKAVCHPTAWDLGKGDFRILMCTKVTMDDFLTAHHEMGHIQYDMAYAAQPF
LLRNGANEGFHEAVGEIMSLSAATPKHLKSIGLLSPDFQEDNETEINFLLKQALTIVGTLPFT
YMLEKWRWMVFKGEIPKDQWMKKWWEMKREIVGVVEPVPHDETYCDPASLFHVSNDYSFIRYY
TRTLYQFQFQEALCQAAKHEGPLHKCDISNSTEAGQKLFNMLRLGKSEPWTLALENVVGAKNM
NVRPLLNYFEPLFTWLKDQNKNSFVGWSTDWSPYADGATSGGGGSAGGSGSGSSGGSSGASGT
GTAGGTGSGSGTGSGGGSGGGSEGGGSEGGGSEGGGSEGGGSEGGGSGGGSESGGSSASNFRV
QPTESIVRFPNITNLCPFGEVFNATRFASVYAWNRKRISNCVADYSVLYNSASFSTFKCYGVS
PTKLNDLCFTNVYADSFVIRGDEVRQIAPGQTGKIADYNYKLPDDFTGCVIAWNSNNLDSKVG
GNYNYLYRLFRKSNLKPFERDISTEIYQAGSTPCNGVEGFNCYFPLQSYGFQPTNGVGYQPYR
VVVLSFELLHAPATVCGPKKSTNLVKNSGHHHHHHTDSLEFIASKLAASGLNDIFEAQKIEWH
EGSGEGQQHHLGGAKQAGDV*

pT7CFE1-MGGG-ACE2-115aa-linker-SARS-CoV-1-RBD-HIS-ybbr-AviTag-Fgɣ

MGGGSSSTIEEQAKTFLDKFNHEAEDLFYQSSLASWNYNTNITEENVQNMNNAGDKWSAFLKE
QSTLAQMYPLQEIQNLTVKLQLQALQQNGSSVLSEDKSKRLNTILNTMSTIYSTGKVCNPDNP
QECLLLEPGLNEIMANSLDYNERLWAWESWRSEVGKQLRPLYEEYVVLKNEMARANHYEDYGD
YWRGDYEVNGVDGYDYSRGQLIEDVEHTFEEIKPLYEHLHAYVRAKLMNAYPSYISPIGCLPA

HLLGDMWGRFWTNLYSLTVPFGQKPNIDVTDAMVDQAWDAQRIFKEAEKFFVSVGLPNMTQGF
WENSMLTDPGNVQKAVCHPTAWDLGKGDFRILMCTKVTMDDFLTAHHEMGHIQYDMAYAAQPF
LLRNGANEGFHEAVGEIMSLSAATPKHLKSIGLLSPDFQEDNETEINFLLKQALTIVGTLPFT
YMLEKWRWMVFKGEIPKDQWMKKWWEMKREIVGVVEPVPHDETYCDPASLFHVSNDYSFIRYY
TRTLYQFQFQEALCQAAKHEGPLHKCDISNSTEAGQKLFNMLRLGKSEPWTLALENVVGAKNM
NVRPLLNYFEPLFTWLKDQNKNSFVGWSTDWSPYADGSEGGGSEGGGSEGGGSEGGGSEGGGS
GGGGATSGGGGSAGGSGSGSSGGSSGASGTGTAGGTGSGSGTGSGGGSGGGSEGGGSEGGGSE
GGGSEGGGSEGGGSGGGSESGGSSARVVPSGDVVRFPNITNLCPFGEVFNATKFPSVYAWERK
KISNCVADYSVLYNSTFFSTFKCYGVSATKLNDLCFSNVYADSFVVKGDDVRQIAPGQTGVIA
DYNYKLPDDFMGCVLAWNTRNIDATSTGNYNYKYRYLRHGKLRPFERDISNVPFSPDGKPCTP
PALNCYWPLNDYGFYTTTGIGYQPYRVVVLSFELLNAPATVCGPKLSTDLIKNQCVNFSGHHH
HHHTDSLEFIASKLAASGLNDIFEAQKIEWHEGSGEGQQHHLGGAKQAGDV*

pT7CFE1-MGGG-ACE2-HIS-ybbr-AviTag-Fgɣ

MGGGSSSTIEEQAKTFLDKFNHEAEDLFYQSSLASWNYNTNITEENVQNMNNAGDKWSAFLKE
QSTLAQMYPLQEIQNLTVKLQLQALQQNGSSVLSEDKSKRLNTILNTMSTIYSTGKVCNPDNP
QECLLLEPGLNEIMANSLDYNERLWAWESWRSEVGKQLRPLYEEYVVLKNEMARANHYEDYGD
YWRGDYEVNGVDGYDYSRGQLIEDVEHTFEEIKPLYEHLHAYVRAKLMNAYPSYISPIGCLPA
HLLGDMWGRFWTNLYSLTVPFGQKPNIDVTDAMVDQAWDAQRIFKEAEKFFVSVGLPNMTQGF
WENSMLTDPGNVQKAVCHPTAWDLGKGDFRILMCTKVTMDDFLTAHHEMGHIQYDMAYAAQPF
LLRNGANEGFHEAVGEIMSLSAATPKHLKSIGLLSPDFQEDNETEINFLLKQALTIVGTLPFT
YMLEKWRWMVFKGEIPKDQWMKKWWEMKREIVGVVEPVPHDETYCDPASLFHVSNDYSFIRYY
TRTLYQFQFQEALCQAAKHEGPLHKCDISNSTEAGQKLFNMLRLGKSEPWTLALENVVGAKNM
NVRPLLNYFEPLFTWLKDQNKNSFVGWSTDWSPYADGSGHHHHHHTDSLEFIASKLAASGLND
IFEAQKIEWHEGSGEGQQHHLGGAKQAGDV*

pET28a_ClfA_N2N3-HIS-ybbr-LPETGG

MATAPVAGTDITNQLTNVTVGIDSGTTVYPHQAGYVKLNYGFSVPNSAVKGDTFKITVPKELNLNG
VTSTAKVPPIMAGDQVLANGVIDSDGNVIYTFTDYVNTKDDVKATLTMPAYIDPENVKKTGNVTLA
TGIGSTTANKTVLVDYEKYGKFYNLSIKGTIDQIDKTNNTYRQTIYVNPSGDNVIAPVLTGNLKPN
TDSNALIDQQNTSIKVYKVDNAADLSESYFVNPENFEDVTNSVNITFPNPNQYKVEFNTPDDQITT
PYIVVVNGHIDPNSKGDLALRSTLYGYNSNIIWRSMSWDNEVAFNNGSGSGDGIDKPVVPEQPSGH
HHHHHGSDSLEFIASKLASLPETGG*

pET28a_MGGG-ybbr-HIS-ddFLN4(C18S)-Fgɣ

MGGGDSLEFIASKLAHHHHHHGSADPEKSYAEGPGLDGGESFQPSKFKIHAVDPDGVHRTDGG
DGFVVTIEGPAPVDPVMVDNGDGTYDVEFEPKEAGDYVINLTLDGDNVNGFPKTVTVKPAPGS
GSGSGSGEGQQHHLGGAKQAGDV*

SARS-CoV-1/2 chimera

CPFGEVFNATKFPSVYAWERKKISNCVADYSVLYNSTFFSTFKCYGVSATKLNDLCFSNVYADSFV
VKGDDVRQIAPGQTGKIADYNYKLPDDFMGCVLAWNTNNIDATSGGNYNYKYRLFRHGKLRPFERD
ISNVPYSADGKPCTPEAFNCYWPLNDYGFQTTNGVGYQPYRVVVLSFE*

TABLES

	MT increments (nm)	**AFM increments (nm)**
ΔRBD	50.7 ± 10.8	48
ΔACE2_1	42.1 ± 5.5	41
ΔACE2_2	45.7 ± 14.0	35
ΔACE2_3	147.6 ± 7.8	148
ΔACE2_combined	191.3 ± 18.7	--

Supplementary Table 1. Increments of high-force transitions in MT and unfolding peaks in the AFM of the SARS-CoV-2 RBD:ACE2 tethered ligand construct. Data are mean and std for 42 molecules in MT and 127 molecules in the AFM. In MT, the ΔACE2_2 and ΔACE2_3 are observed separately only in a small sub-population (8 out of 42 molecules). Mostly they are combined into one step ΔACE2_combined. The large error for the smaller intermediate step is due to imprecisions in the increment measurement due to the short lifetime of this state.

	SARS-CoV-2: ACE2-linker-RBD (85 aa linker)	**SARS-CoV-1: ACE2-linker-RBD (85 aa linker)**
$F_{1/2}$	3.8 ± 0.4 pN	3.2 ± 0.6 pN
Δz (from fit of Equation 1)	10.2 ± 3.7 nm	9.7 ± 1.7 nm
Δz_G (from fit of two Gaussians)	13.5 ± 1.8 nm	11.3 ± 1.7 nm
ΔG_0 ($=\Delta z \times F_{1/2}$)	5.5 ± 2.1 kcal/mol	4.4 ± 1.1 kcal/mol
$t_{0,diss}$	0.07 ± 0.19 s	0.03 ± 0.05 s
$t_{0,bound}$	114.5 ± 278.8 s	19.0 ± 24.8 s
$\Delta G_{0,tau}$ ($= k_BT \times \log(t_{0,diss}/t_{0,bound})$)	4.4 ± 1.7 kcal/mol	3.8 ± 2.0 kcal/mol
Δz_{diss}	7.5 ± 2.6 nm	7.0 ± 1.8 nm
Δz_{bound}	0.4 ± 2.5 nm	1.5 ± 1.6 nm

Supplementary Table 2. Interaction parameters for ACE2 and SARS-CoV-2 or SARS-CoV-1 RBD determined using the tethered ligand assay. Data are the mean and std from N = 12 and 29 molecules, respectively.

SARS-CoV-1	**SARS-CoV-2**
V404	K417
R426	**N439**
T433	G446
Y442	**L455**
L443	**F456**
F460	Y473
P462	**A475**
P470	E484
L472	**F486**
Y484	**Q498**
T487	**N501**
I489	V503

Supplementary Table 3. Mutations on the interface of SARS-CoV-1 and SARS-CoV-2 RBD:ACE2. Residues are labeled according to the corresponding crystal structure (PDB IDs: 2ajf and 6m0j for SARS-CoV-1 and 2, respectively). Residues highlighted in bold were identified as important contacts in the simulations (see “Molecular dynamics simulations” section).

Study	**ACE2 binding to SARS-CoV-1 RBD**	**ACE2 binding to SARS-CoV-2 RBD**	**Method and Comments**
Lan et al. (20)	K_d = 31 nM $k_{sol,off}$ = 4.3×10^{-2} s^{-1} $k_{\mathrm{sol,on}}$ = 1.4×10^{6} $s^{-1}M^{-1}$	K_{d} = 4.7 nM $k_{sol,off}$ = 6.5×10^{-3} s^{-1} $k_{\mathrm{sol,on}}$ = 1.4×10^{6} $s^{-1}M^{-1}$	Surface-plasmon resonance
Shang et al. (55)	K_d =185 nM $k_{sol,off}$ = 3.7×10^{-2} s^{-1} $k_{\mathrm{sol,on}}$ = 2.0×10^{5} $s^{-1}M^{-1}$	K_d =44.2 nM $k_{sol,off}$ = 7.8×10^{-3} s^{-1} $k_{\mathrm{sol,on}}$ = 1.75×10^{5} $s^{-1}M^{-1}$	Surface-plasmon resonance
Starr et al. (56)	K_d =0.12 nM	K_d =0.039 nM	Yeast display screen
Walls *et al.* (57)	K_{d} = 5.0 ± 0.1 nM $k_{sol,off}$ = $(8.7 \pm 5.1)\times10^{-4}$ s^{-1} $k_{\mathrm{sol,on}}$ = $(1.7 \pm 0.7)\times10^{5}$ $s^{-1}M^{-1}$	K_{d} = 1.2 ± 0.1 nM $k_{sol,off}$ = $(1.7 \pm 0.8)\times10^{-4}$ s^{-1} $k_{\mathrm{sol,on}}$ = $(2.3 \pm 1.4)\times10^{5}$ $s^{-1}M^{-1}$	Bio-layer interferometry; uses S protein for both variants
Wang et al. (58)	K_d = 408 ± 11 nM $k_{\mathrm{sol,off}}$ = $(1.9 \pm 0.4)\times10^{-3}$ s^{-1} $k_{\mathrm{sol,on}}$ = $(2.9 \pm 0.2)\times10^{5}$ $s^{-1}M^{-1}$	K_d = 95 ± 7 nM $k_{sol,off}$ = $(3.8 \pm 0.2)\times10^{-3}$ s^{-1} $k_{\mathrm{sol,on}}$ = $(4.0 \pm 0.2)\times10^{4}$ $s^{-1}M^{-1}$	Surface-plasmon resonance; uses S1 domain for SARS-CoV-2
Wrapp et al. (59)	K_{d} = 325 nM $k_{sol,off}$ = 112×10^{-3} s^{-1} $k_{\mathrm{sol,on}}$ = 3.62×10^{5} $s^{-1}M^{-1}$	K_{d} = 14.7 nM $k_{sol,off}$ = 2.76×10^{-3} s^{-1} $k_{\mathrm{sol,on}}$ = 1.88×10^{5} $s^{-1}M^{-1}$	Surface-plasmon resonance; uses ectodomain for both variants

Supplementary Table 4. Equilibrium binding data for ACE2 binding to SARS-CoV-1 or SARS-CoV-2 RBD or S1 proteins. Studies for both ACE2 binding to RBD constructs and to the S protein are included; Wrapp et al. find K_d = 14.7 nM for ACE2 binding to SARS-CoV-2 S and K_d = 34.6 nM for ACE2 binding to SARS-CoV-2 RBD, indicating similar affinities. Similarly, Yang et al. observe similar binding constants and mechanical stabilities for ACE2 binding to either the RBD or S using AFM force spectroscopy (60).

FIGURES

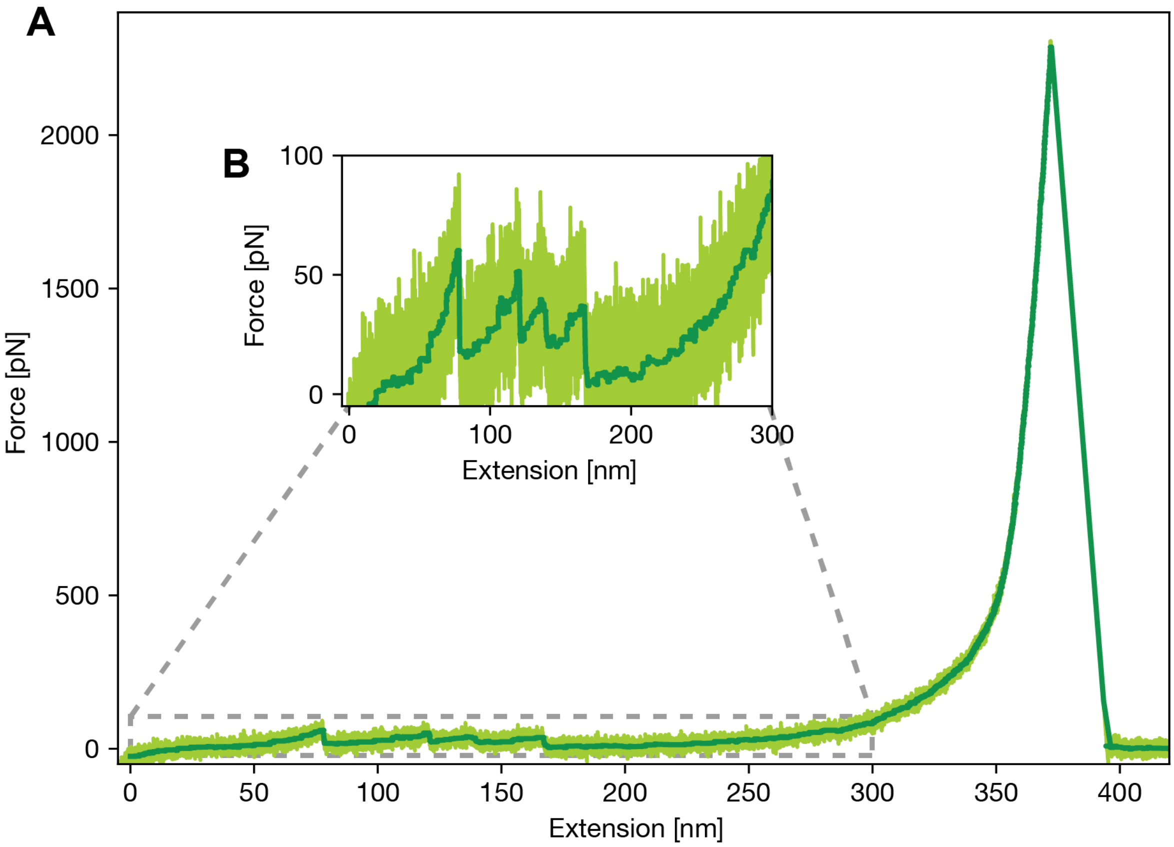

Supplementary Fig. 1: Full force extension curve of the tethered ligand protein construct including the RBD of SARS-CoV-2 and ACE2. A Complete force extension curve showing the entire unfolding and the final rupture of the ClfA:Fgɣ linkage. The full curve shows 4 peaks at lower forces (< 100 pN) and one final rupture at high forces (> 1000 pN). **B** Inset shows the extension range between 0 and 300 nm showing the low force unfolding events attributed to the tethered ligand protein. The first low force peak can be identified as the interface unbinding between SARS-CoV-2 RBD and ACE2 together with a partial unfolding of the RBD. This peak is followed by a trident shaped, three peak pattern that can be assigned to the unfolding of ACE2, see main text.

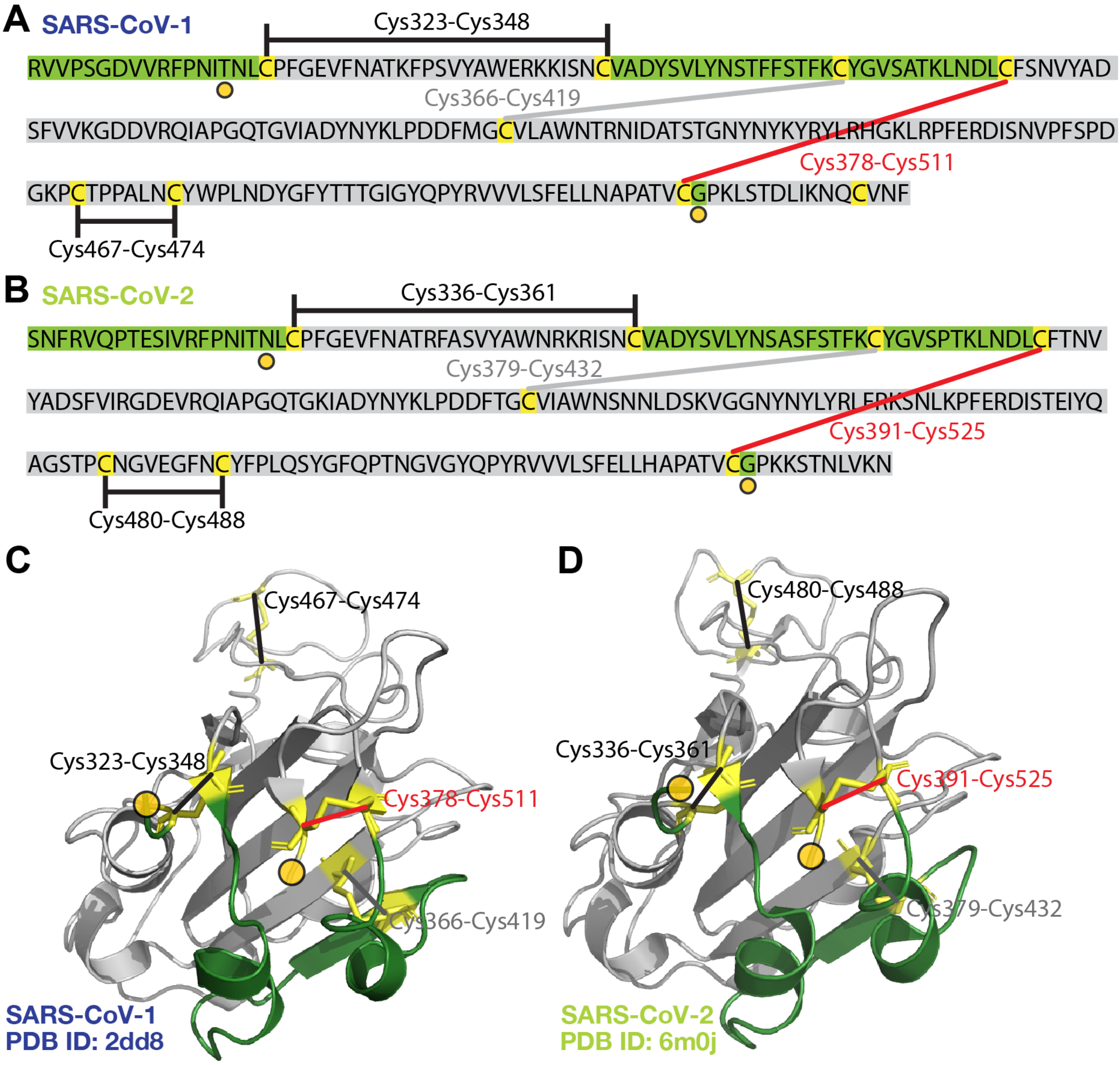

Supplementary Fig. 2 Disulfide bridges shield large parts of the SARS-CoV-1 and SARS-CoV-2 RBD structure. **A** and **B** show the sequence of the SARS-CoV-1 and SARS-CoV-2 RBD with all cysteines highlighted in yellow. The disulfide bridges are indicated as lines between the cysteines in the RBD sequences. These bridges shield parts of the folded protein structure from force and thereby restricts unfolding. The parts of the protein still able to be under force are highlighted in green, shielded parts in grey. The sections under force add up to 51 amino acids (aa, 19 nm for 0.365 nm/aa) for the RBD of SARS-CoV-1 and 54 aa (20 nm for 0.365 nm/aa) for the RBD of SARS-CoV-2 (these include all folded residues as captured in the crystal structure). Some parts of the N-terminus of the RBD used in the tethered ligand protein are probably not folded but will also get released together with the linker increment. The unfolded parts on the C-terminal probably get stretched already in the initial stretching of the linkers for attachment and therefore will not contribute to the length released during the (partial) unfolding of the RBD. In **C** and **D,** the corresponding RBDs of SARS-CoV-1 (PDB ID: 2dd8) and SARS-CoV-2 (PDB ID: 6m0j) are depicted, using the same color code as in **A**, **B** for parts of the protein under force (green), contributing to the increments observed, and parts shielded from unfolding (grey). The orange circles mark the N- and C-terminal end of the crystal structure whereas the sequence in (**A**, **B**) show the entire RBD sequence used in the tethered ligand protein.

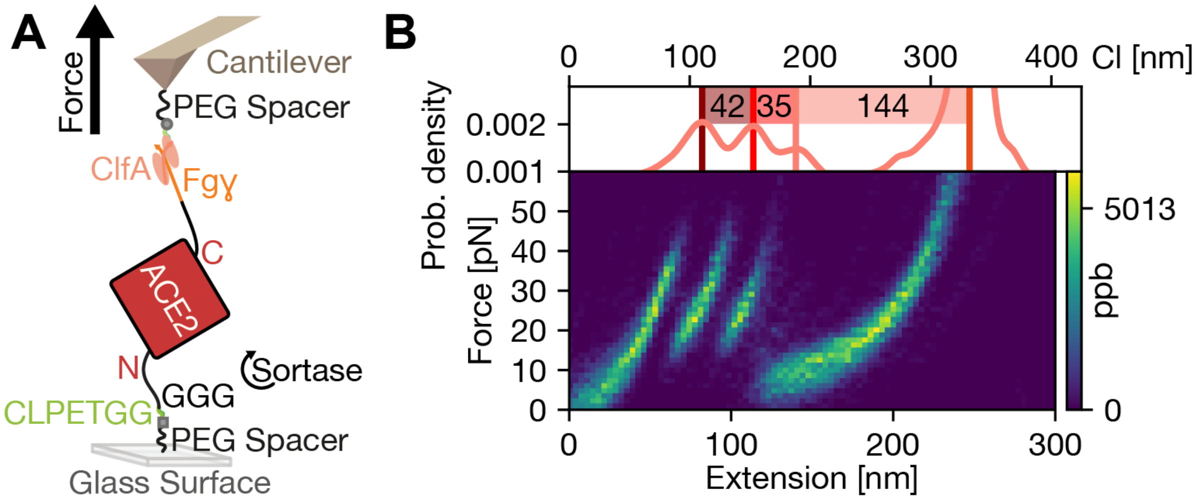

Supplementary Fig. 3 Unfolding of ACE2 by AFM SMFS. A Schematic of the experimental setup pulling on ACE2 which is the same as for the tethered ligand proteins. ACE2 is coupled covalently on an aminosilanized glass surface using heterobifunctional polyethylene glycol (PEG) spacers. The construct is attached in a sortase-mediated reaction to a CLPETGG peptide attached to the maleimide of the PEG spacer. For reversible tethering the Fgɣ tag on the tethered ligand protein can be pulled by a ClfA handle. ClfA is covalently attached to the cantilever by an sfp-mediated reaction, connecting the ybbR tag to a CoA coupled to a PEG spacer on the AFM cantilever. **B** Heatmap created by overlaying 152 aligned AFM unfolding traces of ACE2. The heatmap shows the characteristic ACE2 trident shaped pattern also observed in the full unfolding of the tethered ligand protein. On top an alignment of all contour length transformed density curves is shown. The contour length increments of the ectodomain ACE2 match well with the last increments of the full tethered ligand protein. This allows the assignment of the last three peaks before the final rupture in the complete RBD:ACE2 tethered ligand protein to the unfolding of the ACE2 ectodomain. The characteristic ACE2 unfolding pattern can be used as a fingerprint for identifying single-molecule traces and normalizing force distributions in measurements if they were recorded with different cantilevers.

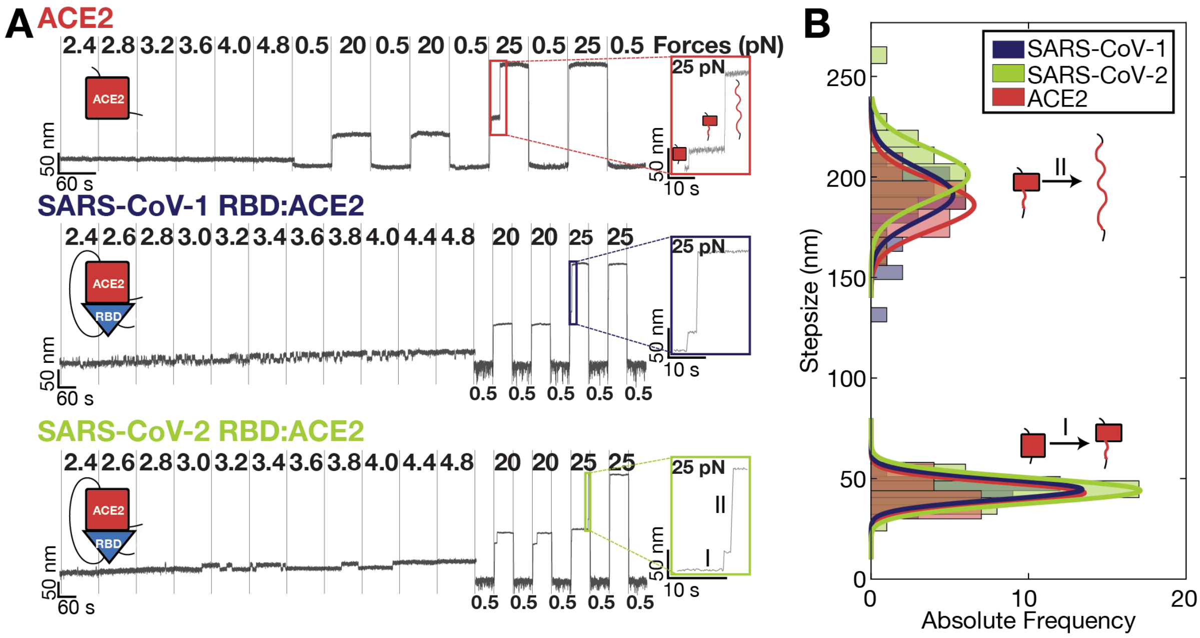

Supplementary Fig. 4. ACE2 unfolding events observed in different constructs in the MT. A Short force ramps and unfolding jumps for single ACE2 (top), SARS-CoV-1 RBD:ACE2 (middle), and SARS-CoV-2 RBD:ACE2 (bottom), measured in MT. Both tethered ligand constructs show equilibrium hopping transitions in the range between 2.4 and 4.8 pN, corresponding to interface opening and partial RBD unfolding. It is apparent that the transitions are much more rapid, i.e. exhibit shorter dwell times, for SARS-CoV-1 compared to SAXS-CoV-2. During the force jumps, all constructs show characteristic two-step unfolding, marking unfolding of the ACE2 domains. **B** Histogram of jump-size distributions of the 2 step-unfolding events, after contour length transformation (with Lp = 0.5 nm) for all constructs shown in **A**. Solid lines represent Gaussian fits to the histograms. Distributions agree very well across the different constructs.

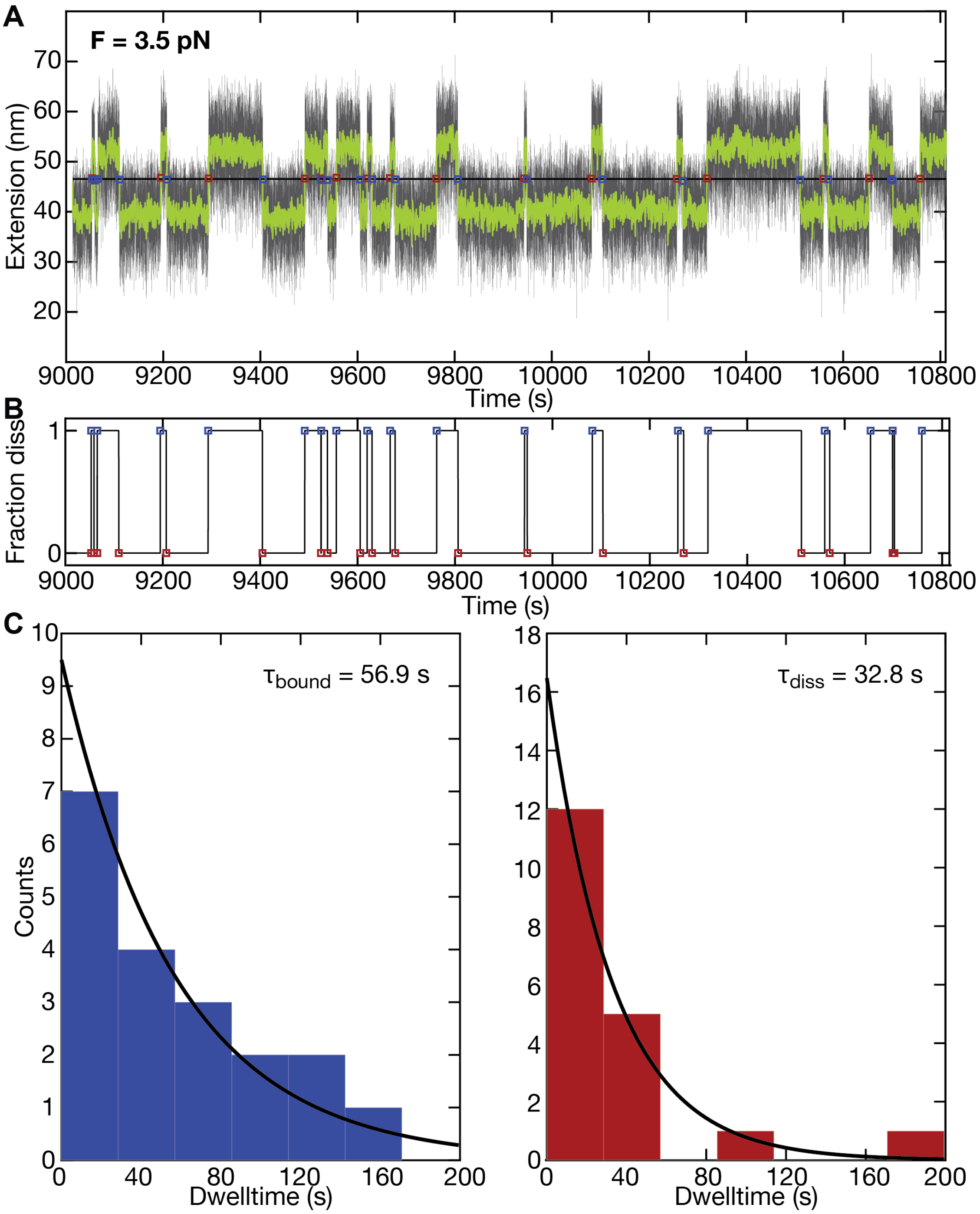

Supplementary Fig. 5. Dwell time analysis of the tethered ligand extension time traces in MT. A Short segment of an extension time trace measured for a SARS-CoV-2 RBD:ACE2 tethered ligand construct at a stretching force of 3.5 pN. Raw data at 72 Hz are shown in black and filtered data (50 frame moving average) are shown in green. Assignment of the dwell times is based on the filtered data. The black horizontal line is the threshold; blue squares indicate the first data point after crossing the threshold from below, i.e. transition from the bound to the dissociated state; red squares indicate the first data point after crossing the threshold from above, i.e. transition from the dissociated to the bound state. **B** Time trace derived from the analysis shown in panel A, indicating the current state of the tethered-ligand system with “1” corresponding to the dissociated state and “0” to the bound state. The time between the transitions between “0” and “1” correspond to the dwell times. **C, D** Histograms of dwell times in the bound state (**C**) and dissociated state (**D**) obtained from the analysis shown in panels **A** and **B**. The dwell times are well described by single exponential fits, shown as solid lines. Insets show the mean dwell times from maximum likelihood fits of the single exponentials.

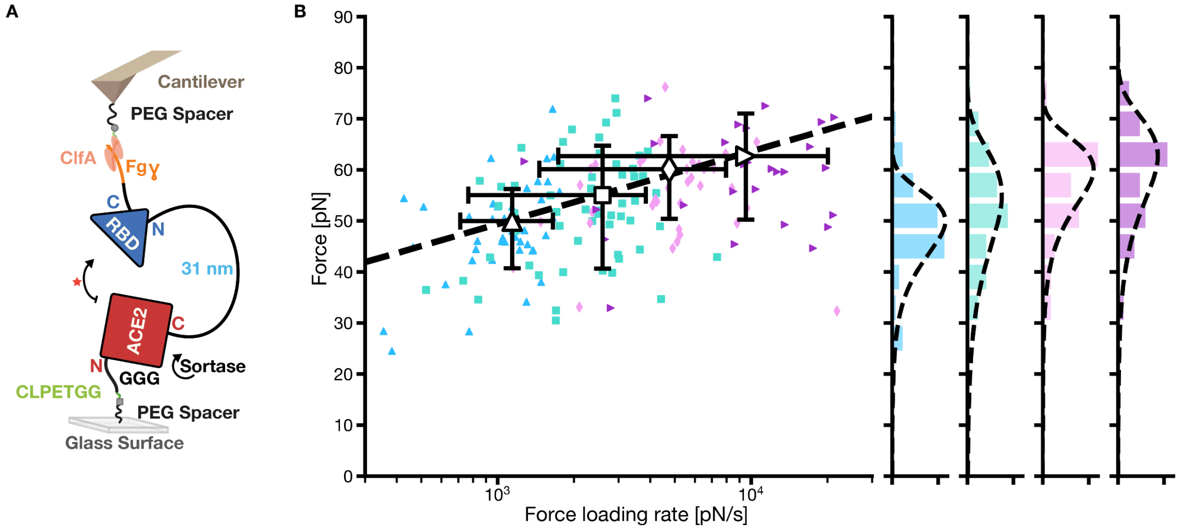

Supplementary Fig. 6. Dynamic force spectrum of the SARS-CoV-2 RBD:ACE2 dissociation (red star). **A** Schematic depiction of the dynamically probed tethered ligand protein consisting of a SARS-CoV-2 RBD and ACE2 joined by a 31 nm linker in the AFM. The attachment strategy is shown together with the probed protein. **B** AFM force spectroscopy measurements were performed with retraction velocities of the sample surface in relation to the cantilever of 0.4 µm/s (blue triangles), 0.8 µm/s (green squares), 1.6 µm/s (lavender diamonds), and 3.2 µm/s (purple forward triangles). The corresponding rupture force histograms are projected on the right and shown with a Bell-Evans fit (thin black dashed lines). A global Bell-Evans fit to the most-probable rupture force and force loading rate of each velocity (large open markers, with errors given as full-width at half maximum for each distribution) is shown as bold dashed line on the left. The fit yields the distance to the transition state of ∆x = 0.67 ± 0.06 nm and zero-force off rate k0 = 0.056 ± 0.04 1/s.

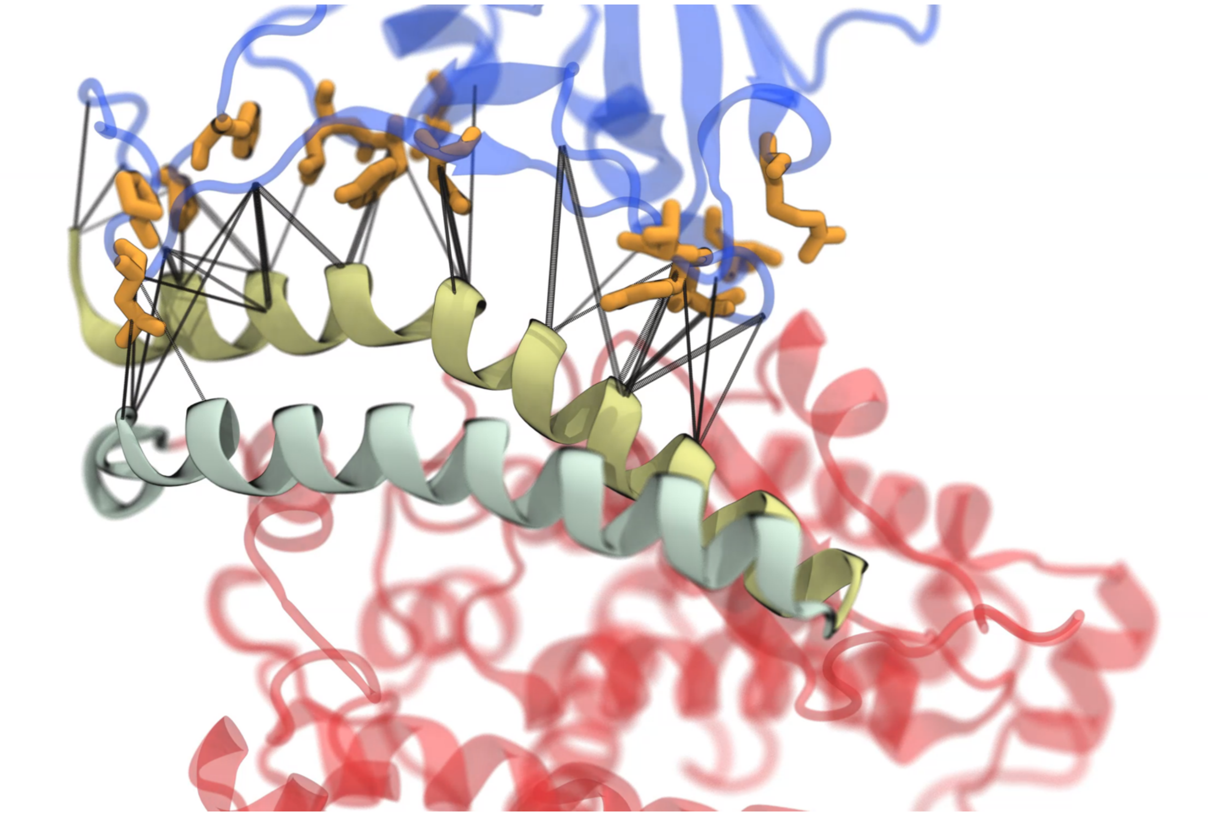

Supplementary Fig. 7. Depiction of the interface between SARS-CoV-1 RBD (blue) and ACE2 (red). The two N-terminal helices from ACE2 are highlighted in solid representations and cyan/green shades. Residues that were modified in the chimera are shown in orange licorice representations. Black lines indicate residues in close proximity, and the thickness of the black lines indicates the correlation between their movements. Under high-force load, most of the correlations between the chimeric RBD and ACE2 occur along the N-terminal helix of ACE2 (green, on top).

REFERENCES

1. T. Komatsu *et al.*, Molecular Cloning, mRNA Expression and Chromosomal Localization of Mouse Angiotensin-converting Enzyme-related Carboxypeptidase (mACE2). *DNA Sequence* **13**, 217-220 (2002).
2. M. A. Marra *et al.*, The Genome Sequence of the SARS-Associated Coronavirus. *Science* **300**, 1399-1404 (2003).
3. F. Li, W. Li, M. Farzan, S. C. Harrison, Structure of SARS Coronavirus Spike Receptor-Binding Domain Complexed with Receptor. *Science* **309**, 1864-1868 (2005).
4. L. F. Milles, H. E. Gaub, Is mechanical receptor ligand dissociation driven by unfolding or unbinding? *bioRxiv* 10.1101/593335, 593335 (2019).
5. F. Wu *et al.*, A new coronavirus associated with human respiratory disease in China. *Nature* **579**, 265-269 (2020).
6. J. L. Hutter, J. Bechhoefer, Calibration of atomic-force microscope tips. *Review of Scientific Instruments* **64**, 1868 1873 (1993).
7. H. J. Butt, M. Jaschke, Calculation of thermal noise in atomic force microscopy. *Nanotechnology* 10.1088/0957-4484/6/1/001/meta (1995).
8. C. R. Harris *et al.*, Array programming with NumPy. *Nature* **585**, 357-362 (2020).
9. J. D. Hunter, Matplotlib: A 2D Graphics Environment. *Comput Sci Eng* **9**, 90-95 (2007).
10. F. Pedregosa *et al.*, Scikit-learn: Machine Learning in Python. *Arxiv* (2012).
11. T. Kluyver *et al.*, *Jupyter Notebooks – a publishing format for reproducible computational workflows* (2016), vol. 20th International Conference on Electronic Publishing, 2016-01-01.
12. E. Evans, K. Ritchie, Dynamic strength of molecular adhesion bonds. *Biophysical journal* **72**, 1541 1555 (1997).
13. E. M. Puchner, G. Franzen, M. Gautel, H. E. Gaub, Comparing Proteins by Their Unfolding Pattern. *Biophysical Journal* **95**, 426-434 (2008).
14. L. Livadaru, R. R. Netz, H. J. Kreuzer, Stretching Response of Discrete Semiflexible Polymers. *Macromolecules* **36**, 3732-3744 (2003).
15. F. Baumann *et al.*, Increasing evidence of mechanical force as a functional regulator in smooth muscle myosin light chain kinase. *eLife* **6**, 621 (2017).
16. J. C. Phillips *et al.*, Scalable molecular dynamics on CPU and GPU architectures with NAMD. *J Chem Phys* **153**, 044130 (2020).
17. W. Humphrey, A. Dalke, K. Schulten, VMD: Visual molecular dynamics. *J Mol Graphics* **14**, 33-38 (1996).
18. J. V. Ribeiro *et al.*, QwikMD — Integrative Molecular Dynamics Toolkit for Novices and Experts. *Sci Rep-uk* **6**, 26536 (2016).
19. R. C. Bernardi *et al.*, Mechanisms of Nanonewton Mechanostability in a Protein Complex Revealed by Molecular Dynamics Simulations and Single-Molecule Force Spectroscopy. *J Am Chem Soc* **141**, 14752-14763 (2019).
20. J. Lan *et al.*, Structure of the SARS-CoV-2 spike receptor-binding domain bound to the ACE2 receptor. *Nature* **581**, 215-220 (2020).
21. B. Webb, A. Sali, Comparative Protein Structure Modeling Using MODELLER. *Curr Protoc Bioinform* **54**, 5.6.1-5.6.37 (2016).
22. S. Hati, S. Bhattacharyya, Impact of Thiol–Disulfide Balance on the Binding of Covid-19 Spike Protein with Angiotensin-Converting Enzyme 2 Receptor. *Acs Omega* **5**, 16292-16298 (2020).
23. R. B. Best *et al.*, Optimization of the Additive CHARMM All-Atom Protein Force Field Targeting Improved Sampling of the Backbone ϕ, ψ and Side-

Chain χ1 and χ2 Dihedral Angles. *J Chem Theory Comput* **8**, 3257-3273 (2012).

24. A. D. MacKerell *et al.*, All-Atom Empirical Potential for Molecular Modeling and Dynamics Studies of Proteins †. *J Phys Chem B* **102**, 3586-3616 (1998).
25. W. L. Jorgensen, J. Chandrasekhar, J. D. Madura, R. W. Impey, M. L. Klein, Comparison of simple potential functions for simulating liquid water. *J Chem Phys* **79**, 926 935 (1998).
26. T. Darden, D. York, L. Pedersen, Particle mesh Ewald: An N·log(N) method for Ewald sums in large systems. *J Chem Phys* **98**, 10089 10092 (1993).
27. J. C. Phillips *et al.*, Scalable molecular dynamics with NAMD. *J Comput Chem* **26**, 1781-1802 (2005).
28. S. Izrailev, S. Stepaniants, M. Balsera, Y. Oono, K. Schulten, Molecular dynamics study of unbinding of the avidin-biotin complex. *Biophysical Journal* **72**, 1568-1581 (1997).
29. C. Schoeler *et al.*, Mapping Mechanical Force Propagation through Biomolecular Complexes. *Nano Lett* **15**, 7370-7376 (2015).
30. M. C. R. Melo, R. C. Bernardi, C. d. l. Fuente-Nunez, Z. Luthey-Schulten, Generalized correlation-based dynamical network analysis: a new high-performance approach for identifying allosteric communications in molecular dynamics trajectories. *J Chem Phys* **153**, 134104 (2020).
31. R. A. Laskowski *et al.*, PDBsum: a web-based database of summaries and analyses of all PDB structures. *Trends Biochem Sci* **22**, 488-490 (1997).
32. A. Löf *et al.*, Multiplexed protein force spectroscopy reveals equilibrium protein folding dynamics and the low-force response of von Willebrand factor. *Proceedings of the National Academy of Sciences* 10.1073/pnas.1901794116 PMID - 31462494, 201901794 (2019).
33. P. U. Walker, W. Vanderlinden, J. Lipfert, Dynamics and energy landscape of DNA plectoneme nucleation. *Physical Review E* **98**, 042412 (2018).
34. J. Lipfert, X. Hao, N. H. Dekker, Quantitative modeling and optimization of magnetic tweezers. *Biophys J* **96**, 5040-5049 (2009).
35. M. T. van Loenhout, J. W. Kerssemakers, I. De Vlaminck, C. Dekker, Non-bias-limited tracking of spherical particles, enabling nanometer resolution at low magnification. *Biophys J* **102**, 2362-2371 (2012).
36. J. P. Cnossen, D. Dulin, N. H. Dekker, An optimized software framework for real-time, high-throughput tracking of spherical beads. *The Review of scientific instruments* **85**, 103712 (2014).
37. A. te Velthuis, J. W. J. Kerssemakers, J. Lipfert, N. H. Dekker, Quantitative Guidelines for Force Calibration through Spectral Analysis of Magnetic Tweezers Data. *Biophysical Journal* **99**, 1292-1302 (2010).
38. I. De Vlaminck, T. Henighan, M. T. van Loenhout, D. R. Burnham, C. Dekker, Magnetic forces and DNA mechanics in multiplexed magnetic tweezers. *PloS one* **7**, e41432 (2012).
39. J. L. Zimmermann, T. Nicolaus, G. Neuert, K. Blank, Thiol-based, site-specific and covalent immobilization of biomolecules for single-molecule experiments. *Nature Protocols* **5**, 975-985 (2010).
40. W. Ott *et al.*, Elastin-like Polypeptide Linkers for Single-Molecule Force Spectroscopy. *ACS Nano* **11**, 6346-6354 (2017).
41. J. Yin, A. J. Lin, D. E. Golan, C. T. Walsh, Site-specific protein labeling by Sfp phosphopantetheinyl transferase. *Nat Protoc* **1**, 280-285 (2006).

42. I. Chen, B. M. Dorr, D. R. Liu, A general strategy for the evolution of bond-forming enzymes using yeast display. *Proceedings of the National Academy of Sciences* **108**, 11399-11404 (2011).
43. E. Durner, W. Ott, M. A. Nash, H. E. Gaub, Post-Translational Sortase-Mediated Attachment of High-Strength Force Spectroscopy Handles. *ACS Omega* **2**, 3064-3069 (2017).
44. S. K. Lai, Y.-Y. Wang, D. Wirtz, J. Hanes, Micro- and macrorheology of mucus. *Adv Drug Deliver Rev* **61**, 86-100 (2009).
45. N. Zhu *et al.*, A Novel Coronavirus from Patients with Pneumonia in China, 2019. *New Engl J Med* **382**, 727-733 (2020).
46. G. R. R.-S. Juan *et al.*, Multi-scale spatial heterogeneity enhances particle clearance in airway ciliary arrays. *Nat Phys* **16**, 958-964 (2020).
47. X. Wang, T. Ha, Defining Single Molecular Forces Required to Activate Integrin and Notch Signaling. *Science* **340**, 991 994 (2013).
48. R. Perez-Jimenez *et al.*, Probing the Effect of Force on HIV-1 Receptor CD4. *ACS Nano* **8**, 10313-10320 (2014).
49. A. F. Oberhauser, P. E. Marszalek, H. P. Erickson, J. M. Fernandez, The molecular elasticity of the extracellular matrix protein tenascin. *Nature* **393**, 181-185 (1998).
50. P. Carl, C. H. Kwok, G. Manderson, D. W. Speicher, D. E. Discher, Forced unfolding modulated by disulfide bonds in the Ig domains of a cell adhesion molecule. *Proceedings of the National Academy of Sciences* **98**, 1565-1570 (2001).
51. P. Maiuri *et al.*, The first World Cell Race. *Curr Biol* **22**, R673-R675 (2012).
52. I. Andreu *et al.*, The force loading rate drives cell mechanosensing through both reinforcement and cytoskeletal softening. *Nat Commun* **12**, 4229 (2021).
53. S. Ghassemi *et al.*, Cells test substrate rigidity by local contractions on submicrometer pillars. *Proceedings of the National Academy of Sciences* **109**, 5328 5333 (2012).
54. T. Wiegand *et al.*, Forces during cellular uptake of viruses and nanoparticles at the ventral side. *Nat Commun* **11**, 32 (2020).
55. J. Shang *et al.*, Structural basis of receptor recognition by SARS-CoV-2. *Nature* **581**, 221-224 (2020).
56. T. N. Starr *et al.*, Deep Mutational Scanning of SARS-CoV-2 Receptor Binding Domain Reveals Constraints on Folding and ACE2 Binding. *Cell* **182**, 1295-1310.e1220 (2020).
57. A. C. Walls *et al.*, Structure, Function, and Antigenicity of the SARS-CoV-2 Spike Glycoprotein. *Cell* **181**, 281-292.e286 (2020).
58. Q. Wang *et al.*, Structural and Functional Basis of SARS-CoV-2 Entry by Using Human ACE2. *Cell* **181**, 894-904.e899 (2020).
59. D. Wrapp *et al.*, Structural Basis for Potent Neutralization of Betacoronaviruses by Single-Domain Camelid Antibodies. *Cell* **181**, 1004-1015.e1015 (2020).
60. J. Yang *et al.*, Molecular interaction and inhibition of SARS-CoV-2 binding to the ACE2 receptor. *Nat Commun* **11**, 4541 (2020).